Materials Research Letters

ISSN: (Print) (Online) Journal homepage: https://www.tandfonline.com/loi/tmrl20

Unique precipitations in a novel refractory Nb-Mo-Ti-Co high-entropy superalloy

N. Yurchenko, E. Panina, Ł. Rogal, L. Shekhawat, S. Zherebtsov & N. Stepanov

To cite this article: N. Yurchenko, E. Panina, Ł. Rogal, L. Shekhawat, S. Zherebtsov & N. Stepanov (2022) Unique precipitations in a novel refractory Nb-Mo-Ti-Co high-entropy superalloy, Materials Research Letters, 10:2, 78-87, DOI: 10.1080/21663831.2021.2022033

To link to this article: https://doi.org/10.1080/21663831.2021.2022033

MATER. RES. LETT.
2022, VOL. 10, NO. 2, 78–87
https://doi.org/10.1080/21663831.2021.2022033

MATERIALS RESEARCH LETTERS
Taylor & Francis
Taylor & Francis Group

ORIGINAL REPORTS

Unique precipitations in a novel refractory Nb-Mo-Ti-Co high-entropy superalloy

N. Yurchenko [a], E. Panina [a], Ł. Rogal[b], L. Shekhawat[a], S. Zherebtsov [a] and N. Stepanov [a]

[a]Laboratory of Bulk Nanostructured Materials, Belgorod National Research University, Belgorod, Russia; [b]Institute of Metallurgy and Materials Science, Polish Academy of Sciences, Krakow, Poland

ABSTRACT

Herein, a novel refractory $Nb_{30}Mo_{30}Ti_{20}Co_{20}$ (at. %) high-entropy superalloy (RHESA) is introduced. Annealing at 1200 °C led to the precipitation of a semi-coherent individual (Co, Ti)-rich B2, (Ti, O)-rich fcc (Ti-rich oxides), and hierarchical B2 + fcc nanoparticles in the (Nb, Mo)-rich RHESA bcc phase. B2 + fcc dispersoids were dominant, and they nucleated heterogeneously because of the coherency ensured by the Baker–Nutting orientation relationship. The emergence of multi-type nanoprecipitates doubled the room-temperature compressive ductility without sacrificing strength. Our study can solve a chief problem of current RHESAs—the low stability of B2 dispersoids at T > 700 °C.

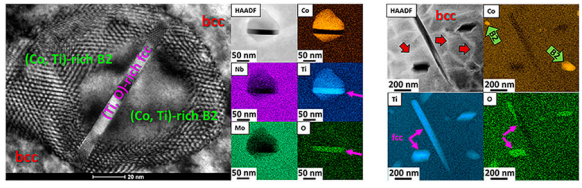

ARTICLE HISTORY
Received 15 November 2021

KEYWORDS
Refractory high-entropy superalloys; hierarchical precipitates; B2 phase; Baker-Nutting orientation relationship; mechanical properties

IMPACT STATEMENT

Multi-type B2, fcc, and B2 + fcc nanoprecipitates balancing mechanical properties of the refractory $Nb_{30}Mo_{30}Ti_{20}Co_{20}$ high-entropy superalloy (RHESA) endow new prospects for application of RHESAs at T ≥ 1200 °C.

Introduction

High-entropy alloys are a novel class of materials with excellent corrosion resistance [1], strength [2], and ductility [3]. Recently, a series of studies showed the formation of a superalloy-like structure comprising coherent body-centred cubic (bcc) and B2 (ordered bcc) phases in refractory Al-containing high-entropy superalloys (RHESAs), which are considered as promising materials for next-generation aerospace applications [4–7]. Two types of mutual arrangements of the phases were reported: (I) B2 matrix + bcc particles and (II) bcc matrix + B2 particles. Type I, most widespread, offers an excellent high-temperature strength but a low room-temperature (RT) ductility [8,9]. Type II is more preferable as it helps achieve more balanced mechanical properties [5].

However, the main drawback of the discrete and compositionally complex Al-rich B2 phase is the low solvus temperature. In numerous RHESAs, B2 particles appear due to spinodal decomposition and dissolve at T > 700 °C [10–13]. To date, only one study has demonstrated that the precipitation of the Al-rich B2 phase is slightly higher than that at 1000 °C [14]. These data points show that the current Al-containing RHESAs cannot compete with the state-of-the-art Ni-based superalloys operating at 1150 °C.

Fortunately, some B2 compounds are prone to precipitation in the refractory metal-based bcc matrix at T ≥ 1000 °C in a controllable fashion [15–17]. Specifically, Knowles et al. [17] showed that the semi-coherent TiFe B2 nanoparticles formed in a W-based matrix of dendritic W-Ti-Fe alloys after solution treatment at 1250 °C for 100 h provided good mechanical properties at 1000 °C. Motivated by the data reported in [15–17], we endeavoured to secure new B2 phases that would expand the potential service temperature of RHESAs to T ≥ 1200 °C.

CONTACT N. Yurchenko yurchenko_nikita@bsu.edu.ru Laboratory of Bulk Nanostructured Materials, Belgorod National Research University, Belgorod 308015, Russia

Supplemental data for this article can be accessed here. https://doi.org/10.1080/21663831.2021.2022033

This study sheds light on the unexpected multi-type precipitation of individual (Co, Ti)-rich B2, (Ti, O)-rich fcc (Ti-rich face-centred cubic oxides), and hierarchical B2 + fcc nanoparticles within the (Nb, Mo)-rich bcc phase of a novel $Nb_{30}Mo_{30}Ti_{20}Co_{20}$ (at. %) RHESA after annealing at 1200 °C, accompanied by a profound increase in the RT compressive ductility.

Materials and methods

A 20 g ingot of the alloy with a nominal composition of $Nb_{30}Mo_{30}Ti_{20}Co_{20}$ was produced by the vacuum arc melting of pure metals ($\geq$ 99.9 wt. %). Rectangular samples measuring $8 \times 8 \times 3$ mm^3 were cut from the as-cast ingot. Some samples were encapsulated in vacuumed (10^{-2} Torr) quartz tubes filled with titanium chips to prevent oxidation during annealing at 1200 °C for 24 h (further denoted as an annealed state), followed by water quenching. The microstructure of the alloy was studied for the as-cast and annealed states using scanning electron microscopy (SEM) and energy-dispersive X-ray spectroscopy (EDS) with an FEI Quanta 600 FEG scanning electron microscope equipped with an energy-dispersive detector. Data on the actual chemical composition (metals) of the alloy measured by SEM-EDS analysis and the content of impurities (oxygen, nitrogen, and hydrogen) determined by inert gas fusion are given in Table 1.

Transmission electron microscopy (TEM; JEOL JEM-2100 and Tecnai G2 F20 transmission electron microscopes) was used for in-depth microstructural investigations, and integrated EDS was conducted for micro-chemical analysis. For TEM examinations, thin foils were prepared using a Tenupol-5 twin-jet electropolisher with an electrolyte containing sulfuric acid and methanol (1:9) at 10 °C and 15 V. We attempted to perform TEM analyses immediately after the thin foil preparation to minimise atmospheric exposure. Selected area electron diffraction (SAED) patterns were used for phase identification and orientation relationship analysis.

For mechanical tests in the as-cast and annealed states, rectangular samples measuring $5 \times 3 \times 3$ mm^3 were used. Uniaxial compression tests were performed at RT using an Instron 5882 test machine. Testing was carried out at an initial strain rate of 10^{-4} s^{-1} until the fracture of the specimens. True stress–true strain curves were obtained using procedures described elsewhere [18].

Results

A typical microstructure of the $Nb_{30}Mo_{30}Ti_{20}Co_{20}$ alloy is shown in Figure 1. The combined SEM-EDS and TEM-SAED analyses of the as-cast and annealed states revealed similar dendritic microstructures comprising two dominant phases: bright-grey (Nb, Mo)-rich islands with a bcc (*W-prototype; cI2; Im-3 m*) crystal structure and dark-grey (Co, Ti)-rich interlayers with a B2 (*CsCl-prototype; cP2; Pm-3 m*) crystal structure; some coarse round/needle-shaped B2 particles were embedded in the bcc islands (Figures 1(a, b), TableS1, Supplementary Material). We also found a minor (Ti, O)-rich phase with an fcc (*NaCl-prototype; cF8; Fm-3 m*) crystal structure. It was located within the B2 interlayers, predominantly along the bcc/B2 interfaces, as sporadic, micron-sized, black particles (highlighted with pink arrows in Figures 1(a, b), TableS1, Supplementary Material). The volume fractions of the bcc, B2, and fcc phases in the as-cast and annealed states were approximately 70%, 29%, and 1%, respectively. Only a negligible diversity in the chemical compositions and lattice parameters of the constitutive phases between the as-cast and annealed states was noted (Table S1, Supplementary Material).

However, an investigation of the annealed alloy at higher magnifications revealed profuse secondary dispersoids inside the bcc islands that were absent in the as-cast state, while the B2 interlayers were precipitate-free (Figure 2(a)). Many nanoparticles consisted of segments, namely a cubic core and an elongated tail, with different Z-contrasts (denoted by white arrows as hierarchical precipitates in Figure 2(a)). In-depth characterisation using high-angle annular dark-field scanning TEM (STEM-HAADF) confirmed the occurrence of hierarchical nanoparticles with diverse Z-contrasts (some of them are marked with white arrows in Figure 2 (b)). According to STEM-EDS mapping, these precipitates consisted of (Co, Ti)-rich ($Nb_{14.2}Mo_{12.5}Ti_{32.9}Co_{40.4}$) and Ti-rich ($Nb_{4.9}Mo_{3.4}Ti_{90.8}Co_{0.9}$) segments with various

Table 1. Actual chemical composition of the $Nb_{30}Mo_{30}Ti_{20}Co_{20}$ alloy.

Elements, at.%						
Nb	Mo	Ti	Co	Oxygen, ppm	Nitrogen, ppm	Hydrogen, ppm
28.8 ± 0.2	32.8 ± 1.6	19.4 ± 0.8	19.0 ± 1.0		As-cast	
				392 ± 17	49 ± 12	22 ± 7
					Annealed	
				403 ± 15	54 ± 10	29 ± 5

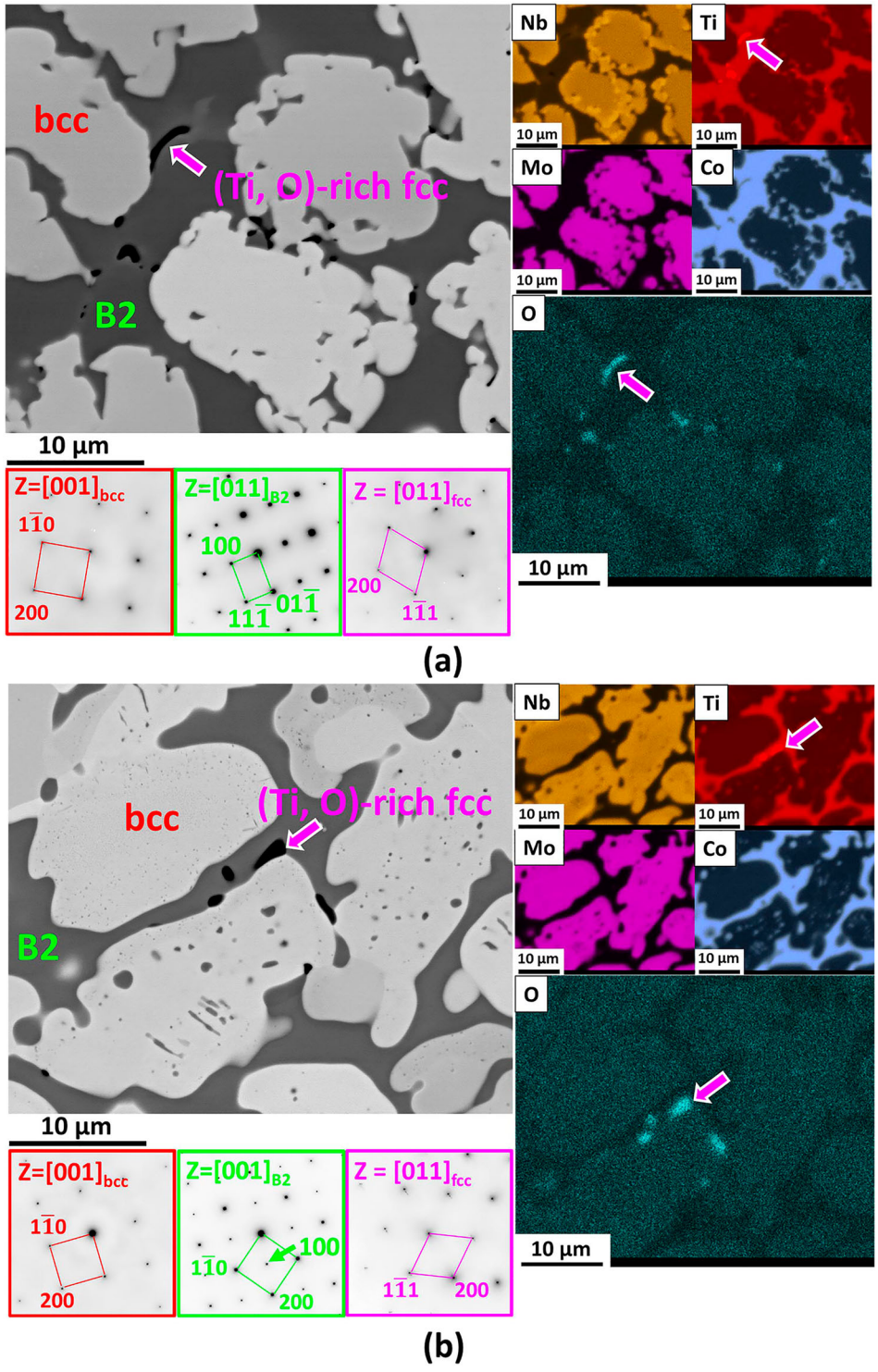

Figure 1. A typical microstructure of the $Nb_{30}Mo_{30}Ti_{20}Co_{20}$ alloy in the as-cast (a) and annealed (b) states: SEM-BSE images, SEM-EDS maps, and SAED patterns recorded from $[001]_{bcc}$, $[011]_{B2}$ (as-cast state) or $[001]_{B2}$ (annealed state), and $[011]_{fcc}$ zone axes of the corresponding phases showing the dendritic microstructure consisting of (Nb, Mo)-rich bcc islands, (Co, Ti)-rich B2 network, and (Ti, O)-rich fcc particles.

morphologies and sizes (Figure 2). The Ti-rich segments predominantly appeared as thin (~7–40 nm) and elongated (~45–130 nm) plates. Their long axes were encompassed by or adjoined to one of the sides of semi-circular/irregularly shaped (Co, Ti)-rich segments; meanwhile, the plate rims remained bordered to the bcc

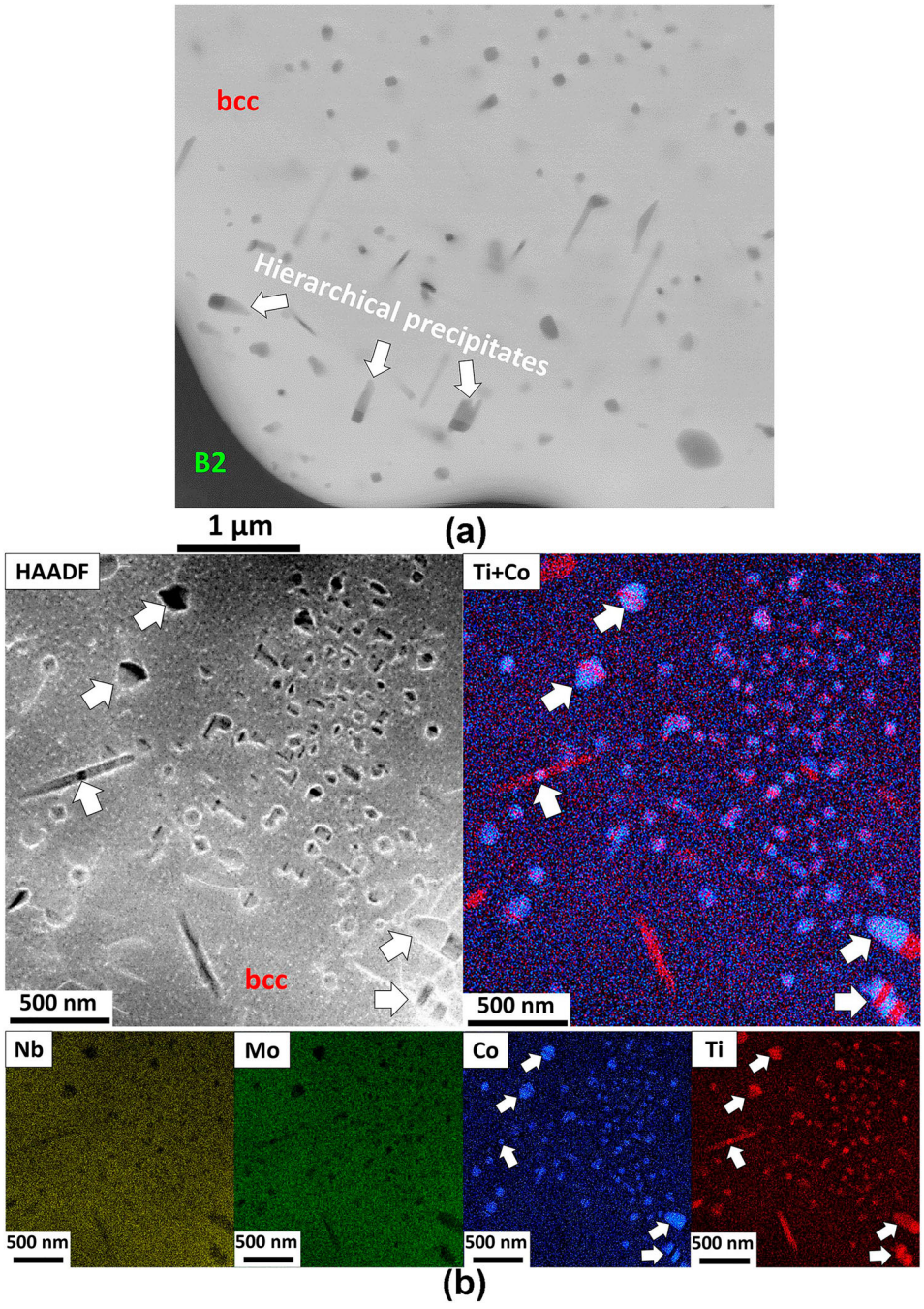

Figure 2. Characterisation of the bcc islands of the annealed $Nb_{30}Mo_{30}Ti_{20}Co_{20}$ alloy: (a) – magnified SEM-BSE image of typical bcc islands demonstrating the embedded dispersed particles of different morphology and Z-contrast denoted as 'hierarchical precipitates'; (b) STEM-HAADF and STEM-EDS analyses showing the presence of hierarchical nanoprecipitates (some characteristic particles highlighted with white arrows) composed of Ti-rich and (Co, Ti)-rich segments inside the (Nb, Mo)-rich matrix.

matrix. Occasionally, small (~ 40–50 nm) round-shaped (Co, Ti)-rich segments were embedded in relatively large (~ 500 nm in width) Ti-rich needles.

A more detailed investigation of the hierarchical nanoprecipitates was performed using high-resolution TEM (HRTEM) and STEM-EDS (Figure 3). The (Co, Ti)-rich segments possessed a B2 (*CsCl-prototype; cP2; Pm-3 m*; $a = 0.3052 \pm 0.0029$ nm) crystal structure. Meanwhile, the Ti-rich segments had an fcc (*NaCl-prototype; cF8; Fm-3 m*; $a = 0.4293 \pm 0.0014$ nm) crystal structure and contained a considerable amount of oxygen, similar to that of the initial fcc particles (Figures 1(a) and 3(a, b)). We identified the orientation relationships (ORs) between the bcc matrix and different segments of the hierarchical B2 + fcc particles (Figure 3(b)). The B2 segments adopted a cube-on-cube $001_{bcc} \parallel$

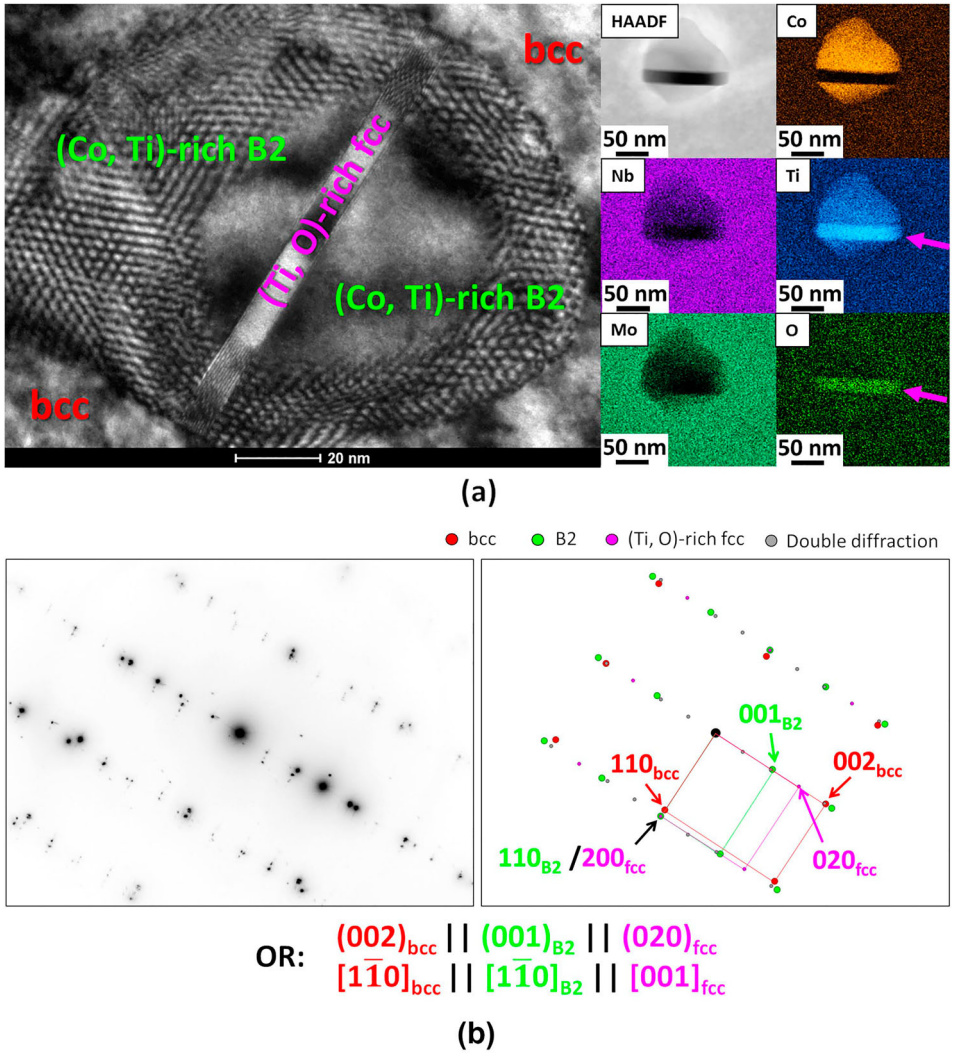

Figure 3. Detailed TEM characterisation of hierarchical nanoparticles in the annealed $Nb_{30}Mo_{30}Ti_{20}Co_{20}$ alloy: (a) – HRTEM image demonstrating a typical hierarchical precipitate consisting of a one (Ti, O)-rich fcc plate and two (Co, Ti)-rich B2 segments inside the bcc matrix; (b) – SAED taken simultaneously from the bcc matrix and hierarchical B2 + fcc precipitates and sketch illustrating the ORs between the phases.

001_{B2}, $<110>_{bcc} \parallel <110>_{B2}$ OR, which was previously observed in numerous refractory alloys, including RHE(S)As [4,13,15,17,19,20]. In turn, the fcc segments obeyed the Baker–Nutting (B-N) OR $001_{bcc} \parallel 001_{fcc}$, $<110>_{bcc} \parallel <100>_{fcc}$, which is typical of carbides, nitrides, or oxides precipitated in steels [21–23] and other bcc alloys [24–26]. Notably, the B-N OR was also found between the fcc and B2 segments.

Apart from the prevailing hierarchical particles, we detected sparse individual (Co, Ti)-rich B2 and (Ti, O)-rich fcc nanoprecipitates (Figures 2 and 4(a)). The latter exhibited various morphologies (plate-, cubic, or rhombic-like), most probably due to different orientations with respect to the thin foil cross-section (the so-called stereological effect). HRTEM investigations of the typical plate-like fcc (Figure 4(b)) and round/irregularly shaped B2 (Figure S1, Supplementary Material) dispersoids showed that they held similar (as their hierarchical counterparts) ORs relative to the bcc matrix. Multiple dislocations (highlighted with red arrows in the HAADF-STEM image in Figure 4(a)) around the nanoprecipitates were also observed.

The significant effect of annealing on mechanical properties must be noted. Figure 5(a) displays the compressive true stress–true strain curves of the $Nb_{30}Mo_{30}Ti_{20}Co_{20}$ alloy in the as-cast and annealed states tested at RT. Compared to the as-cast state, the annealed alloy showed a slightly lower yield stress ($YS_{as-cast}$ = 1185 MPa vs. $YS_{annealed}$ = 1120 MPa) but a notably enhanced ductility ($e_{as-cast}$ = 0.095 vs. $e_{annealed}$ = 0.26). Post-mortem microstructure investigations near the main crack revealed the absence of multiple

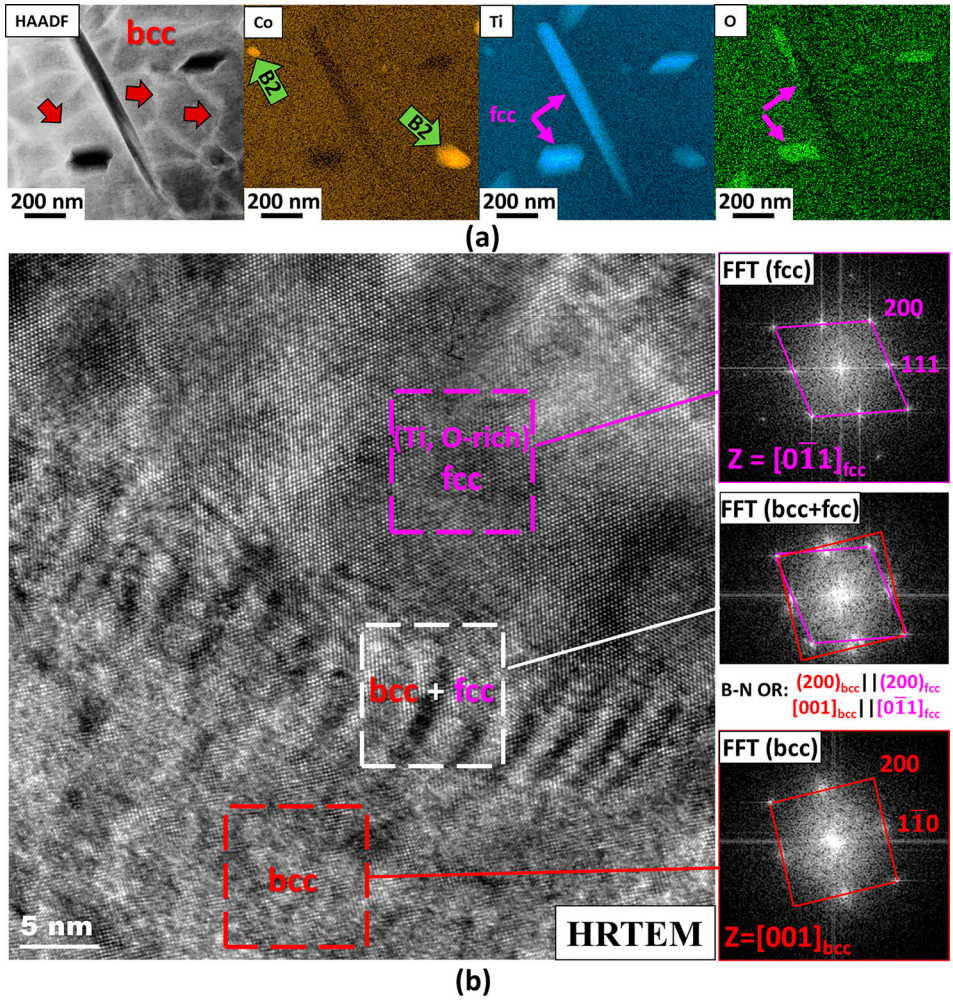

Figure 4. Detailed TEM characterisation of individual nanoparticles in the annealed $Nb_{30}Mo_{30}Ti_{20}Co_{20}$ alloy: (a) – HAADF-STEM image and STEM-EDS maps showing the individual (Co, Ti)-rich B2 (denoted with light-green arrows) and (Ti, O)-rich fcc (denoted with pink arrows) precipitates and dislocations (denoted with dark-red arrows) in the bcc matrix; (b) – HRTEM image illustrating the typical interface between the bcc matrix and plate-like individual fcc particle supporting by Fast Fourier Transforms (FFTs) taken from regions denoted and the deciphered B-N OR between the phases.

secondary cracks in the annealed alloy, in contrast to that of the as-cast alloy (Figures 5(b, c)).

Discussion

Formation mechanisms of multi-type precipitates

The $Nb_{30}Mo_{30}Ti_{20}Co_{20}$ alloy with an initial multi-phase (Nb, Mo)-rich bcc + (Co, Ti)-rich B2 + (Ti, O)-rich fcc microstructure, which could be reasonably predicted by thermodynamic modelling (Figure S2, Supplementary Material), experienced complex precipitation behaviour after annealing at 1200 °C. In the dominant dendritic bcc phase, we found a variety of secondary particles: individual (Co, Ti)-rich B2 and (Ti, O)-rich fcc, as well as abundant hierarchical B2 + fcc. Different groups of researchers have already reported on the occurrence of individual B2 dispersoids after proper heat treatment in a bcc matrix of refractory alloys, including RHESAs [4,5,7,13–15,17,19,27]; however, no data exist on the 1200 °C-B2 precipitates in RHESAs. In addition, few studies on RHE(S)As informed about O-rich dispersoids, and these inclusions were usual constituents in mechanically alloyed RHE(S)As [28–30] but were absent in arc-melted counterparts. Moreover, this is the first observation of hierarchical B2 + fcc nanoparticles in such alloys. This encourages us to provide a plausible explanation for the possible formation mechanism(s) of multi-type precipitates in the $Nb_{30}Mo_{30}Ti_{20}Co_{20}$ RHESA.

Several studies have mentioned the presence of O-rich fcc particles in the structure of arc-melted Nb-based refractory alloys [24,31–33], albeit with diverse data: Leonard et al. [24] and Senkov et al. [33] considered them as oxides, while Ma et al. [31,32] insisted on the

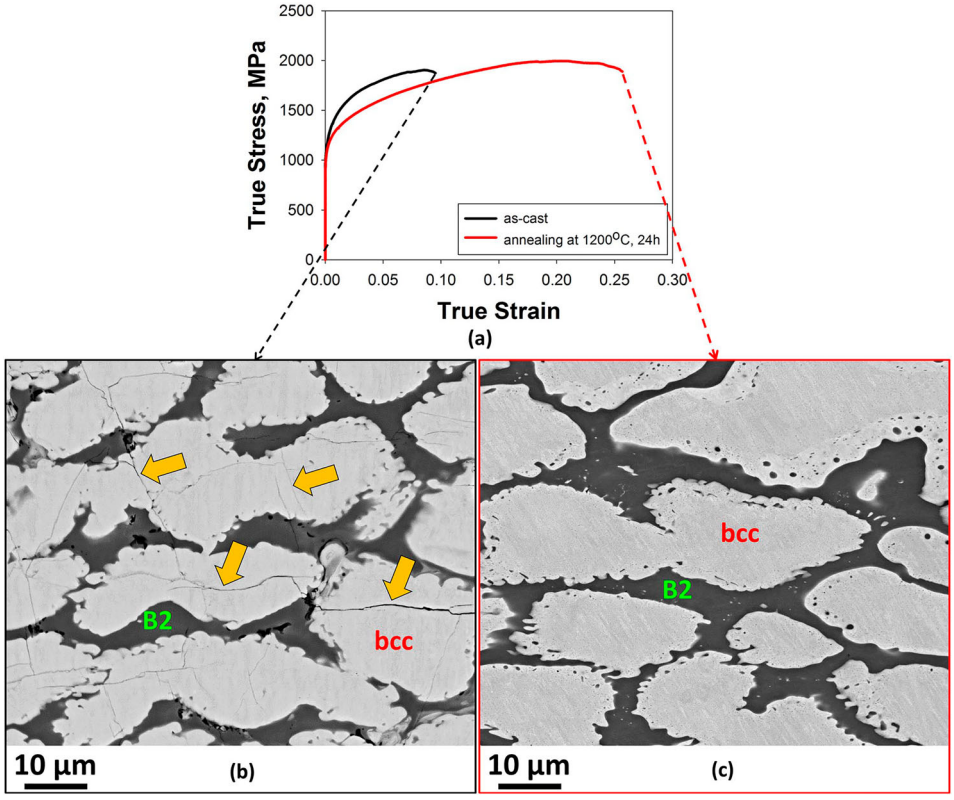

Figure 5. Mechanical properties and post-mortem microstructure investigations of the $Nb_{30}Mo_{30}Ti_{20}Co_{20}$ alloy in the as-cast and annealed states: (a) – true stress – true strain curves obtained during compression test at RT; (b) and (c) – SEM-BSE images of the as-cast (b) and annealed (c) specimens after RT compression test. Orange arrows in Figure 5(b) show the presence of multiple secondary cracks in the microstructure of the as-cast specimen. The compression axis is vertical.

non-oxide origin. In the studied alloy, based on the chemical composition (mostly oxygen distribution in EDS maps) (Figures 3(a) and 4(a), Table S1, Supplementary Material), crystal structure prototype (Figures 3(b) and 4(b)), and adopted B-N OR (different from that reported in [31,32]), we assumed both the fcc segments of hierarchical B2 + fcc nanoparticles and the individual fcc dispersoids to be Ti-rich oxides. The initial micron-sized fcc particles (Figure 1) could also be Ti-rich oxides, although we did not identify the ORs held. In steels, oxides often act as sites for the heterogeneous nucleation of ferrite [34–36]. The latter process can be mitigated by numerous factors, of which the lattice disregistry is considered one of the main parameters. According to the Bramfitt theory [37], the lower the lattice mismatch between the inclusion and the nuclei, the higher the formation potency. For this, the inclusion and the nuclei should have similar lattices and obey simple ORs. In our case, the Ti-rich oxides and the B2 phase seem to satisfy both criteria: they possess cubic crystal structures, adopt the B-N OR, and hold the B-N and cube-on-cube ORs relative to the bcc matrix (Figures 3(b) and 4(b)). These ORs were used to evaluate the lattice misfit parameter $\bar{\delta}$, as per the formula [37]:

$$\bar{\delta} = \sum_{i=1}^{3} \frac{1}{3} \frac{|(d_{[uvw]^i_{bcc/B2}} \cos\theta) - d_{[uvw]^i_{B2/fcc}}|}{d_{[uvw]^i_{B2/fcc}}} \times 100\%, \quad (1)$$

where $[uvw]_{bcc}$, $[uvw]_{B2}$, and $[uvw]_{fcc}$ are the Miller indices for the low-index crystal directions of the bcc phase, B2 phase, and Ti-rich oxide, respectively; $d_{[uvw]bcc}$, $d_{[uvw]B2}$, and $d_{[uvw]fcc}$ are the interatomic spacing along $[uvw]_{bcc}$, $[uvw]_{B2}$, and $[uvw]_{fcc}$, respectively, and θ is the angle between $[uvw]_{bcc}$, $[uvw]_{B2}$, and $[uvw]_{fcc}$. The calculation parameters are presented in Table S2 (Supplementary Material).

From the derived data, it can be interpreted that the B2 phase or the Ti-rich oxide shows relatively low planar ($\bar{\delta}^{B2}_{bcc} = 5.603\%$) or linear ($\delta^{\langle 100\rangle_{fcc}}_{\langle 110\rangle_{bcc}} = 6.173\%$) lattice disregistry to the bcc matrix, indicating semi-coherent interfaces and almost equal abilities for homogeneous formation (Table S2, Supplementary Material). In turn, both B2 dispersoids and Ti-rich oxides are more suitable nucleation sites for each other than the bcc

matrix because of the coherency along the $<110>_{B2}$ / $<100>_{fcc}$ directions ($\delta^{\langle 100\rangle_{fcc}}_{\langle 110\rangle_{B2}} = 0.54\%$) (Table S2, Supplementary Material). This means that if any of these phases appear first in the bcc matrix, the heterogeneous formation of another phase will be greatly alleviated. Unfortunately, the precipitation sequence of the B2 phase and Ti-rich oxides remains debatable. From the energetic point, the independent nucleation of these phases requires large concentration fluctuations: a simultaneous local increase in the content of Ti and Co or Ti and O is needed for the corresponding B2 phase or Ti-rich oxide formation (Table S1, Supplementary Material). Nevertheless, the experimentally observed higher fraction of hierarchical B2 + fcc nanoparticles suggests the dominance of the heterogeneous precipitation mechanism over the homogeneous one.

It should also be noted that the emergence of stable (Co, Ti)-rich B2 dispersoids (and, possibly, Ti-rich oxides) in the $Nb_{30}Mo_{30}Ti_{20}Co_{20}$ alloy can be anticipated even at T ≥ 1200 °C, according to the CALPHAD data (Figure S2, Supplementary Material; [38]), thereby significantly outperforming the temperature limit (< 1000 °C) of the current RHESAs. However, to obtain a complete picture of the complex phase transformations in the studied alloy, heat treatments at different temperatures and durations should be performed. These are the goals of future studies.

Effect of precipitates on mechanical properties

Considering the slight alterations in the chemical compositions of the constitutive phases after annealing (Table S1, Supplementary Material), we suggest other factors resulting in negligible softening and more than two-fold ductility increment in the $Nb_{30}Mo_{30}Ti_{20}Co_{20}$ alloy (Figure 5). In refractory metals and alloys, impurities profoundly affect their mechanical properties [39–41]. Specifically, a high oxygen content in a solid solution increases the strength but leads to inevitable brittleness [42–47]. In rare cases, controllable O-doping has been shown to harden without significant ductility loss [48,49]. For RHEAs, however, only two systematic studies have been conducted to elucidate the effect of O on the mechanical performance. Chen et al. observed a rather typical behaviour in $ZrTiHfNb_{0.5}Ta_{0.5}O_x$ RHEAs when O was added: the alloys became stronger at the expense of the RT compression ductility [50]. Meanwhile, Lei et al. revealed that the doping of a TiZrHfNb RHEA with 2 at. % of O conquered the strength-ductility trade-off by forming ordered complexes, changing the planar slip to wavy; however, a higher O content deteriorated the properties [51].

Interestingly, oxygen-induced embrittlement and hardening can be removed by a simple heat treatment. Liu and Inouye [42] returned the initial level of ductility to an oxidised TZM alloy by annealing at T ≥ 1400 °C. DiStefano and Chitwood [45] successfully utilised the same procedure for an oxygen-contaminated Nb-1Zr alloy. Both studies attributed annealing-invoked ductilising to the formation of incoherent (Ti, Zr)- [42] or Zr-rich [45] oxides, which scavenge excess O from the solid solution. A similar heat treatment response appears for the $Nb_{30}Mo_{30}Ti_{20}Co_{20}$ alloy: the compressive ductility increased when semi-coherent Ti-rich oxides were precipitated in the bcc matrix.

Lastly, we can roughly estimate the solid solution softening effect of O in the annealed $Nb_{30}Mo_{30}Ti_{20}Co_{20}$ alloy. The as-cast and annealed states showed a comparative bulk oxygen content of ~400 ppm (or ~0.2%) (Table 1). Assuming that all oxygen was in the solid solution(s) or in the Ti-rich oxides in the as-cast or annealed states, respectively, and following the dependencies between the O content and the *YS* found in [42,45,48,50,51] (Figure S3 and Table S3, Supplementary Material), the softening caused by O gettering was evaluated to be $\Delta\sigma_{oxygen}$ ~100 MPa. In turn, the decrease in strength could be partially compensated by precipitation hardening. The overall contribution of the multi-type B2, fcc, and B2 + fcc dispersoids to the strength was estimated according to the Ashby–Orowan equation (Supplementary Material, formula (S1) [52]) as $\Delta\sigma_{precipitates}$ ~45 MPa. This indicates a good correlation between the calculated oxygen depletion-induced solid solution softening–precipitation hardening trade-off (~55 MPa) and the experimentally observed *YS* decrease ($\Delta YS_{as-cast-annealed} = 65$ MPa).

The above data show that proper heat treatment resulting in the appearance of multi-type nanoparticles, such as B2 and Ti-rich oxides, both in the form of individual and hierarchical dispersoids, can be a promising strategy to improve the strength-ductility combination in different RHE(S)As. However, further research is required in this direction.

Conclusions

In summary, in the search for novel RHESAs with a possible operating temperature of ≥ 1200 °C, we introduced the $Nb_{30}Mo_{30}Ti_{20}Co_{20}$ alloy. It had a dendritic microstructure and comprised two dominant (Nb, Mo)-rich bcc and (Co, Ti)-rich B2 phases and traces of a (Ti, O)-rich fcc phase (Ti-rich fcc oxides). Annealing at 1200 °C led to the precipitation of multi-type semi-coherent nanoparticles, namely scarce individual (Co, Ti)-rich B2, (Ti, O)-rich fcc (Ti-rich oxides), and

profuse hierarchical B2 + fcc inside the bcc phase. The dominance of the hierarchical B2 + fcc dispersoids was ascribed to the favourable heterogeneous nucleation due to the perfect crystallographic matching ensured by the Baker–Nutting orientation relationship. Oxygen trapping by the Ti-rich oxides was recognised as the most probable reason for the greater than two-fold improvement in the compressive RT ductility of the annealed alloy. Our study is the first demonstration of B2 nanoparticle precipitation in RHESAs at 1200 °C and the evasion of the oxygen-induced embrittlement of RHE(S)As by forming Ti-rich oxides.

Acknowledgements

This work was carried out using the equipment of the Joint Research Center of Belgorod State National Research University «Technology and Materials». The authors also thank Dr A. Belyakov, Belgorod National Research University, for fruitful discussions and Dr D. Shaysultanov for aid in an alloy's ingot preparation.

Data availability statement

The data that support the findings of this study are available from the corresponding author upon reasonable request.

Disclosure statement

No potential conflict of interest was reported by the author(s).

Funding

This work was supported by the Russian Science Foundation grant number 19-79-30066.

ORCID

N. Yurchenko http://orcid.org/0000-0002-6078-8325
E. Panina http://orcid.org/0000-0002-9440-887X
S. Zherebtsov http://orcid.org/0000-0002-1663-429X
N. Stepanov http://orcid.org/0000-0003-2476-3953

References

[1] Zhang Y, Zuo TT, Tang Z, et al. Microstructures and properties of high-entropy alloys. Prog Mater Sci. 2014;61:1–93.
[2] Lee C, Chou Y, Kim G, et al. Lattice-distortion-enhanced yield strength in a refractory high-entropy alloy. Adv Mater. 2020;32:1–9.
[3] Pang J, Zhang H, Zhang L, et al. Ductile $Ti_{1.5}ZrNbAl0.3$ refractory high entropy alloy with high specific strength. Mater Lett. 2021;290:129428.
[4] Jensen JK, Welk BA, Williams REA, et al. Characterisation of the microstructure of the compositionally complex alloy $Al_1Mo_{0.5}Nb_1Ta_{0.5}Ti_1Zr_1$. Scr Mater. 2016;121:1–4.
[5] Soni V, Senkov ON, Gwalani B, et al. Microstructural design for improving ductility of an initially brittle refractory high entropy alloy. Sci Rep. 2018;8:1–10.
[6] Schliephake D, Medvedev AE, Imran MK, et al. Precipitation behaviour and mechanical properties of a novel $Al_{0.5}MoTaTi$ complex concentrated alloy. Scr Mater. 2019;173:16–20.
[7] Miracle DB, Tsai MH, Senkov ON, et al. Refractory high entropy superalloys (RSAs). Scr Mater. 2020;187:445–452.
[8] Senkov ON, Isheim D, Seidman DN, et al. Development of a refractory high entropy superalloy. Entropy. 2016;18:1–13.
[9] Senkov ON, Jensen JK, Pilchak AL, et al. Compositional variation effects on the microstructure and properties of a refractory high-entropy superalloy $AlMo_{0.5}NbTa_{0.5}TiZr$. Mater Des. 2018;139:498–511.
[10] Soni V, Gwalani B, Senkov ON, et al. Phase stability as a function of temperature in a refractory high-entropy alloy. J Mater Res. 2018;33:3235–3246.
[11] Soni V, Gwalani B, Alam T, et al. Phase inversion in a two-phase, BCC + B2, refractory high entropy alloy. Acta Mater. 2020;185:89–97.
[12] Soni V, Senkov ON, Couzinie J-P, et al. Phase stability and microstructure evolution in a ductile refractory high entropy alloy $Al_{10}Nb_{15}Ta_5Ti_{30}Zr_{40}$. Materialia. 2020;9:100569.
[13] Whitfield TE, Pickering EJ, Owen LR, et al. The effect of Al on the formation and stability of a BCC – B2 microstructure in a refractory metal high entropy superalloy system. Materialia. 2020;13:100858.
[14] Laube S, Schellert S, Tirunilai AS, et al. Microstructure tailoring of Al-containing compositionally complex alloys by controlling the sequence of precipitation and ordering. Acta Mater. 2021;218:117217.
[15] Ghosh G, Olson GB. Integrated design of Nb-based superalloys: Ab initio calculations, computational thermodynamics and kinetics, and experimental results. Acta Mater. 2007;55:3281–3303.
[16] Knowles AJ, Jones NG, Messé OMDM, et al. Phase equilibria in the Fe-Mo-Ti ternary system at 1000 C. Int J Refract Met Hard Mater. 2016;60:160–168.
[17] Knowles AJ, Dye D, Dodds RJ, et al. Tungsten-based bcc-superalloys. Appl Mater Today. 2021;23:101014.
[18] Senkov ON, Rao SI, Butler TM, et al. Ductile Nb alloys with reduced density and cost. J Alloys Compd. 2019;808:151685.
[19] Wang Z, Jin D, Han J, et al. Microstructures and mechanical properties of Al-Ti-Zr-Nb-Ta-Mo-V refractory high-entropy alloys with coherent B2 nanoprecipitation. Cryst. 2021;11:833.
[20] Yurchenko N, Panina E, Shaysultanov D, et al. Refractory high entropy alloy with ductile intermetallic B2 matrix/hard bcc particles and exceptional strain hardening capacity. Materialia. 2021;20:101225.
[21] Ishikawa F, Takahashi T, Ochi T. Intragranular ferrite nucleation in medium-carbon vanadium steels. Metall Mater Trans A. 1994;25(5):929–936.
[22] Shanmugam S, Misra RDK, Mannering T, et al. Impact toughness and microstructure relationship in niobium- and vanadium-microalloyed steels processed with varied cooling rates to similar yield strength. Mater Sci Eng A. 2006;437:436–445.

[23] Furuhara T, Shinyoshi T, Miyamoto G, et al. Multiphase crystallography in the nucleation of intragranular ferrite on MnS + V(C, N) complex precipitate in Austenite. ISIJ Int. 2003;43:2028–2037.
[24] Leonard KJ, Busby JT, Hoelzer DT, et al. Nb-Base FS-85 alloy as a candidate structural Material for space reactor applications: effects of thermal aging. Metall Mater Trans A. 2009;40(4):838–855.
[25] Vishwanadh B, Arya A, Tewari R, et al. Formation mechanism of stable NbC carbide phase in Nb-1Zr-0.1C (wt.%) alloy. Acta Mater. 2018;144:470–483.
[26] Ikehata H, Mayweg D, Jägle E. Grain refinement of Fe–Ti alloys fabricated by laser powder bed fusion. Mater Des. 2021;204:109665.
[27] Wang Q, Han J, Liu Y, et al. Coherent precipitation and stability of cuboidal nanoparticles in body-centered-cubic $Al_{0.4}Nb_{0.5}Ta_{0.5}TiZr_{0.8}$ refractory high entropy alloy. Scr Mater. 2021;190:40–45.
[28] Lv S, Zu Y, Chen G, et al. A multiple nonmetallic atoms co-doped CrMoNbWTi refractory high-entropy alloy with ultra-high strength and hardness. Mater Sci Eng A. 2020;795:140035.
[29] Liu Q, Wang G, Sui X, et al. Ultra-fine grain Ti_xVNbMoTa refractory high-entropy alloys with superior mechanical properties fabricated by powder metallurgy. J Alloys Compd. 2021;865:158592.
[30] Zhao B, Chen G, Lv S, et al. Doping N/O impurities into a MoNbTiWZr refractory multi-principal element alloy and the strengthening mechanism. J Mater Eng Perform. 2021;2021:1–11.
[31] Ma X, Guo X, Fu M, et al. Precipitation and martensitic transformation of fcc-Ti in Nb–Ti–Si based ultrahigh temperature alloys. Intermetallics. 2016;70:17–23.
[32] Ma X, Guo X, Fu M, et al. In-situ TEM observation of hcp-Ti to fcc-Ti phase transformation in Nb-Ti-Si based alloys. Mater Charact. 2018;142:332–339.
[33] Senkov ON, Rao SI, Butler TM, et al. Microstructure and properties of Nb-Mo-Zr based refractory alloys. Int J Refract Met Hard Mater. 2020;92:105321.
[34] Enomoto M. Nucleation of phase transformations at intragranular inclusions in steel. Met Mater. 1998;4(2): 115–123.
[35] Sarma DS, Karasev A V, Jönsson PG. On the role of nonmetallic inclusions in the nucleation of acicular ferrite in steels. ISIJ Int. 2009;49:1063–1074.
[36] Mills AR, Thewlis G, Whiteman JA. Nature of inclusions in steel weld metals and their influence on formation of acicular ferrite. Mater Sci Technol. 1987;3: 1051–1061.
[37] Bramfitt BL. The effect of carbide and nitride additions on the heterogeneous nucleation behavior of liquid iron. Metall Trans. 1970;1:2958.
[38] Davydov A V, Kattner UR, Josell D, et al. Determination of the CoTi congruent melting point and thermodynamic reassessment of the Co-Ti system. Metall Mater Trans A. 2001;32(9):2175–2186.
[39] Wadsworth J, Nieh TG, Stephens JJ. Recent advances in aerospace refractory metal alloys. Int Mater Rev. 1988;33:131–150.
[40] El-Genk MS, Tournier JM. A review of refractory metal alloys and mechanically alloyed-oxide dispersion strengthened steels for space nuclear power systems. J Nucl Mater. 2005;340:93–112.
[41] Knabl W, Leichtfried G, Stickler R. Refractory metals and refractory metal alloys. Springer Handbooks. Springer International Publishing; 2018. p. 307–337.
[42] Liu CT, Inouye H. Internal oxidation and mechanical properties of TZM-Mo alloy. Metall Mater Trans B. 1974;5(12):2515–2525.
[43] Donoso JR, Reed-Hill RE. Slow strain-rate embrittlement of niobium by oxygen. Metall Trans A. 1976;7(7):961–965.
[44] Shiraishi H, Furuya K, Watanabe R. Change in solute oxygen level and loss of ductility of niobium during oxidation in imperfect vacuum conditions. J Less Common Met. 1979;63:147–158.
[45] DiStefano JR, Chitwood LD. Oxidation and its effects on the mechanical properties of Nb–1Zr. J Nucl Mater. 2001;295:42–48.
[46] Kim WY, Tanaka H, Kasama A, et al. Effect of carbon on the tensile properties of Nb–Mo–W alloys at 1773K. J Alloys Compd. 2002;333:170–178.
[47] Yang PJ, Li QJ, Tsuru T, et al. Mechanism of hardening and damage initiation in oxygen embrittlement of body-centred-cubic niobium. Acta Mater. 2019;168:331–342.
[48] Yang PJ, Li QJ, Han WZ, et al. Designing solid solution hardening to retain uniform ductility while quadrupling yield strength. Acta Mater. 2019;179:107–118.
[49] Zhang J, Han WZ. Oxygen solutes induced anomalous hardening, toughening and embrittlement in body-centered cubic vanadium. Acta Mater. 2020;196:122–132.
[50] Chen Y, Li Y, Cheng X, et al. Interstitial strengthening of refractory $ZrTiHfNb_{0.5}Ta_{0.5}O_x$ ($x = 0.05, 0.1, 0.2$) high-entropy alloys. Mater Lett. 2018;228:145–147.
[51] Lei Z, Liu X, Wu Y, et al. Enhanced strength and ductility in a high-entropy alloy via ordered oxygen complexes. Nature. 2018;563:546–550.
[52] Gladman T. Precipitation hardening in metals. Mater Sci Technol. 1999;15:30–36.